Chemical short-range order in $Fe_{50}Mn_{30}Co_{10}Cr_{10}$ high-entropy alloy

D. Liu [a, b, f], Q. Wang [c, f], J. Wang [a], X.F. Chen [a, b], P. Jiang [a], F.P. Yuan [a, b], Z.Y. Cheng [d, **], E. Ma [e, ***], X.L. Wu [a, b, *]

[a] State Key Laboratory of Nonlinear Mechanics, Institute of Mechanics, Chinese Academy of Sciences, Beijing 100190, China
[b] School of Engineering Science, University of Chinese Academy of Sciences, Beijing 100049, China
[c] Science and Technology on Surface Physics and Chemistry Laboratory, P. O. Box 9-35, Jiangyou 621908, China
[d] National Center of Electron Microscopy in Beijing, School of Materials Science and Engineering, Tsinghua University, Beijing 100084, China
[e] Center for Alloy Innovation and Design (CAID), State Key Laboratory for Mechanical Behavior of Materials, Xi'an Jiaotong University, Xi'an 710049, China

ARTICLE INFO

ABSTRACT

Chemical short-range order (CSRO) is generally possible in concentrated solid solutions and currently of considerable interest for multi-principal element alloys. However, a convincing demonstration of CSRO has been challenging and achieved thus far only for ternary medium-entropy alloys such as VCoNi. Here, we report definitive proof of CSRO in a quaternary face-centered-cubic $Fe_{50}Mn_{30}Co_{10}Cr_{10}$ high-entropy alloy, acquired from systematic electron microscopy experiments. The evidence includes extra diffuse disks in nano-beam electron diffraction patterns, images in state-of-the-art aberration-corrected scanning transmission electron microscope, as well as compositional profiles across neighboring atomic planes/columns in atomic-resolution chemical maps. The CSRO regions are found to occupy an areal fraction of 20% and have dimensions on a sub-nanometer scale. This length scale, as well as the diffraction features of the CSRO, are different from those of intermetallic compound precipitates; as such, the CSRO is not a growing stage of a nucleated second phase, the precipitation of which has been dealt with previously in classical alloys. We further conducted a spatial correlation analysis of the concentrations in atomic columns in the chemical map, enabling us to uncover a general tendency toward nearest-neighbor chemical ordering, specifically, preference for unlike species (such as Fe−Mn) and avoidance for like-species (such as Fe−Fe). The persistence of this trend, the same as that found in VCoNi MEA, recently, is somewhat intriguing for a high-entropy alloy in which all the constituent elements are similar in atomic size and have rather a small enthalpy of mixing.

© 2021 The Author(s). Published by Elsevier Ltd. This is an open access article under the CC BY-NC-ND license (http://creativecommons.org/licenses/by-nc-nd/4.0/).

1. Introduction

High and medium-entropy alloys (H/MEAs) are multiple-principal-element solid solutions [1−14], retained to room temperature often as a single-phase. In such concentrated solutions, the complex chemical interaction among constituent species is very likely to produce chemical short-range order (CSRO) to some degree/extent [12−32], unless the alloy is directly quenched from a very high temperature where entropy-driven intermixing overwhelms enthalpy-driven ordering [26]. CSRO refers to the

preference/avoidance of some of the constituent species in the alloy away from the atomic fractions expected for random mixing, but the chemical order is so short-ranged that it prevails only in the first and the next couple of nearest-neighbor atomic shells around the atom at the center. While the presence of CSROs is expected to influence the properties of the alloy, such as the dynamics of defects [14,26], a convincing identification of CSRO is difficult because of the need to acquire detailed information on the atomic scale [12−14,33−37]. Direct observation of the CSRO inside a transmission electron microscope (TEM) [13,14,33−37] is possible, for example, using dark-field imaging, when the character of CSRO, and its degree/extent, gives rise to extra reflection(s) in the selected area electron diffraction pattern [14,33−36]. Specifically, in the selected area electron diffraction pattern of a local region, the CSRO may give off extra reflection(s), i.e. *diffuse*, usually in the form of a disk [14,33,36] with a diameter substantially larger than that of normal Bragg spots [14,33]. Such diffraction evidence in reciprocal

space would demonstrate that the regions with local chemical order (LCO) are present in real space with their sizes on the scale of 1 nm. Previous studies have followed this route and claimed the presence of regions in some alloys with the presence of short-range order (SRO) [38,39]. But for the H/MEAs, the search for and understanding of CSRO is only in its rudimentary stage, encountering several difficulties, as outlined in the following.

First, the H/MEAs are usually solid solutions composed of species that are close in the periodic table of elements [1,2] and, hence, in their electronegativity, such that the enthalpy of mixing of the alloys may not be sufficiently large in magnitude to drive pronounced and wide-spread chemical ordering/clustering. Second, the constituent species are similar in atomic number (and hence atomic scattering factor and atomic size), such that the extra reflections corresponding to the CSROs (with a moderate volume density) would be of rather low intensity. Third, the CSROs are very small in size, typically below *1 nm* in size, and may vary in their configurations from one spatial location to another leading to highly diffuse reflections that are hard to be distinguished from the background. As diffraction signals are very weak or utterly invisible, identifying CSROs in high-entropy alloys (HEAs) *via* traditional dark-field imaging would be challenging.

One way to increase the chances of observing CSRO is to use the nano-beam diffraction, which substantially improves the signal-to-noise ratio. There have been reports that used energy-filtered dark-field imaging, striving to make CSROs discernible [13,14,40]. However, even with these efforts, the firm evidence of CSROs in HEAs is still lacking [13]. One factor contributing to this difficulty, first of all, is that an appropriate zone axis needs to be found to detect extra reflections in electron diffraction. This is non-trivial because of the lack of knowledge as to how the various elements pack in the CSRO to occupy lattice planes/sites in the H/MEA solution. Generally, extra scattering arising from CSROs can be visible in one specific zone axis but becomes much weaker or even totally disappear in others [41] as the diffraction intensity varies strongly with crystallographic orientations [33]. On this account, it is necessary to check diffraction patterns under various zone axes. This is clearly demonstrated in very recent experiments on face-centered cubic (fcc) MEA [14], where the extra diffuse reflections from CSROs are observed at $\frac{1}{2}$ $[\bar{3}11]$ positions under the [112] zone axis but not under the routinely used [110] beam direction. Second, there appears to be confusion as how to interpret the extra reflections seen in experiments. For HEAs [31,32], and even for earlier reports of SROs in alloys [38], what had been claimed as evidence of SROs were often rather sharp diffraction spots indicative of long-range order. Even those 'diffuse reflections' indicating the so-called SRO [39] are not so diffuse after all, likely corresponding to ordered regions that extend to well above 1 nm − beyond the realm of CSRO. In other words, the chemically ordered entities they reported can be better characterized as LCO, albeit perhaps metastable structures less than a few nanometers in diameter in at least some of the three dimensions (such as nano-lamellar plates). These entities were claimed as 'short-range order' [31,39], only in the (somewhat misleading) sense that they are still tiny in some dimensions compared with normally observed (second-phase) precipitates. Such LCOs were reported for the CrCoNi MEA (extra-diffraction spots appearing at $\frac{1}{2}$ $[\bar{1}10]$ positions) [13] and for the fcc phase of dual-phase Fe−Mn−Co−Cr HEA [31] (extra diffraction spots at the $\frac{1}{2}$ $[\bar{3}11]$ positions under the [112] zone axis, reportedly corresponding to 2 nm regions). Also, in the FeCrMnCoNi HEA [32], in some concentrated alloys related to HEAs, such as Ni-based alloy [38] and high-Mn Transformation-induced-plasticity (TRIP) steel [39], as well as in some non-HEA cases [40], extra reflections emerge at either $\frac{1}{2}$ $[\bar{3}11]$ or $\frac{1}{3}$ $[\bar{4}22]$ positions with the [112] zone axis or [111] zone axis. However, in all these cases, the

extra diffraction spots are too sharp, or at least insufficiently diffuse, to be associated with the sub-nanometer CSRO discussed in this article. In other words, these entities have grown to dimensions that are long-range orders but on the smallest side; LCOs start from CSROs, but the chemical ordering has evolved/expanded to a spatial extent that clearly corresponds to a long-range-ordered crystal, across regions at least a few nanometers in one or more dimensions. In some cases, the LCOs reported may be identified as equilibrium (or metastable) intermetallic compound crystals with dimensions (see the reported TEM images [31,32]) far beyond their critical nuclei radius. Unfortunately, the authors did not decipher the atomic configurations of these LCOs [12,13,31,32,38−40]. In other words, what they observed can be an early stage of precipitation. As H/MEAs are metastable solutions, phase separation (and compositional decomposition) upon long-duration aging is not a surprise. Note that the stages of second phase precipitation (going through various stages, sizes and morphology) are what has been commonly encountered in conventional alloys, which is a different question from the CSRO inherent in the (as-prepared) single-phase solid solution we are focusing here. In fact, the CSRO we are talking about is incipient chemical order that can be entirely different from the chemical order found in any known compounds (e.g. see in the phase diagram at some specific compositions in the alloy system in question).

In this article, we focus on the question of detecting *bona fide* CSRO in HEAs. There was convincing experimental evidence of CSRO only in a ternary VCoNi MEA but not for higher-order HEAs. Here, we look into if and what kind of CSRO would emerge in a quaternary, non-equiatomic Fe−Mn−Co−Cr HEA [6,31]. Although in some cases CSROs may be so dilute and diverse that they may escape detection altogether with the TEM techniques today, we demonstrate in the following that in the $Fe_{50}Mn_{30}Co_{10}Cr_{10}$ HEA the diffraction/dark-field imaging approach, in combination with atom-resolution chemical composition mapping, can indeed reveal CSRO in a HEA. Interestingly, while Cr, Mn, Fe and Co are neighbors in the periodic table of elements with only minor differences in atomic size and small enthalpy of mixing, when mixed in the $Fe_{50}Mn_{30}Co_{10}Cr_{10}$ HEA they still exhibit CSRO along the line of unlike-pair preference and unlike-pair avoidance as nearest neighbors.

2. Methods

2.1. Materials, testing, and observation techniques

The Fe−Mn−Co−Cr HEA was produced by arc-melting pure elements (all >99.9% purity) and subsequently casting into a 150 mm diameter iron mold under an argon atmosphere. To ensure homogeneity, the ingot was re-melted five times and flipped multiple times. The ingot was then multi-directionally hot-forged and hot-rolled at the temperature of 1150 °C to the plates with the dimension of $12 \times 80 \times 800$ mm^3, and then, vacuum heat-treated in at 1150 °C for 24 h for homogenization, followed by rapidly quenching in water. The plate was hot-rolled with 85% thickness reduction and finally cold-rolled with 30% thickness reduction. The final thickness of the sheets was 1 mm. The actual composition, determined using chemical analysis, was 52.7% Fe, 28.1% Mn, 10.0% Co, and 9.2% Cr, all in atomic %, only slightly deviating from the designed composition of $Fe_{50}Mn_{30}Co_{10}Cr_{10}$.

Tensile specimens were cut along the rolling direction, with a gauge cross-section of 4×1 mm^2 and 15 mm in length. The uniaxial tensile straining was performed using MTS 793 machine at room temperature and a strain rate of 5×10^{-4} s^{-1}, with an extensometer across the 10 mm initial gauge length. Before tensile straining, recrystallization annealing was conducted at a temperature of 760 °C for 10 min and 600 °C for 1 h, respectively.

The constituent phase characterization was made using X-ray diffraction with Cu target operating at 9 kW (Rigaku Smart Lab X-ray diffractometer with the Cu-Kα radiation at 45 kV and 200 mA). The samples were scanned through the 2θ range from 40 to 100 deg with a step size of 0.01 deg and a counting time of 1 s. The microstructure before and after tensile straining was then observed using the electron backscattered diffraction (EBSD) imaging in a ZEISS Supra 55 scanning electron microscope with an EBSD detector. The samples for EBSD were mechanically polished first, followed by electro-polishing in a solution of 5% perchloric and 95% alcohol at 30 V. Atom probe tomography (APT) (LEAP 4000X HR) was used to investigate the elemental distribution in nanoscale. The APT tip was taken from an EBSD sample using the focused ion beam technique (FEI Helios Nanolab 300).

The foils for TEM observations were thinned and polished to 50 μm thick from the sheets before and after tensile straining. Foils were then punched to discs of 3 mm in diameter, and perforated finally in a twin-jet electro-polishing using a solution of 8 vol% perchloric acid and 92 vol% alcohol at the temperature of −25 °C and voltage of 30 V. Both atomic-resolution TEM and high-angle annular dark-field (HAADF) observations were carried out in an aberration-corrected scanning transmission electron microscope (STEM, FEI Titan Cubed Themis G2 300) operated at 300 kV, equipped with a Super-X EDS with four windowless silicon-drift detectors. The nanobeam electron diffraction was performed under the TEM microprobe mode with an electron beam diameter of ~35 nm. The count rate was in the range of 180−500 cps in quantitative energy dispersive X-ray spectroscopy (EDS) mapping with atomic resolution. The dwell time was 5 μs per pixel. Each EDS mapping, with a map size of 512 × 512 pixels, took roughly 1 h to reach the high signal-to-noise ratio.

2.2. Spatial correlation analysis

In a recent work [14], a set of spatial pair correlation coefficients has been developed to quantitatively gauge the ordering from the experimental EDS line profiles. The spatial pair correlation coefficient, $C_{A-B}(r)$, between an A-B element pair is defined as [14],

$$C_{A-B}(r) = \frac{\langle (x_A(0) - \langle x_A \rangle)(x_B(r) - \langle x_B \rangle) \rangle}{\sqrt{\langle (x_A - \langle x_A \rangle)^2 \rangle}\sqrt{\langle (x_B - \langle x_B \rangle)^2 \rangle}} \quad (1)$$

where $x_A(0)$ is the concentration of element A at reference position (0) in an EDS line profile and $x_B(r)$ is the concentration of B at the location a distance of r away, and $\langle x_A \rangle$ and $\langle x_B \rangle$ are the average composition of A and B, respectively.

A positive $C_{A-B}(r)$ indicates that the compositions with r apart tend to vary synchronously. A negative $C_{A-B}(r)$ signals a negative correlation, i.e., the two are inversely correlated. When A and B are of the same species, $C_{A-B}(r)$ characterize the self-correlation of that element at r; when not, they characterize the cross-correlation among different species. In the form of the covariance normalized by the product of standard deviations (Eq. (1)), $C_{A-B}(r)$ falls in [-1,1], indicating the strength of correlation. In particular, the $C_{A-B}(r)$ at r^* is quite informative in revealing the 1st-neighbor CSRO, where r^* is the distance between adjacent projected columns when projecting a (111) plane along the [112] zone axis. As shown in a schematic of Ref. [14], when projecting along the [112] zone axis, four 1st-neighbors will be located at a distance of r^* from the center atom (two on each side), and statistically, the $C_{A-B}(r^*)$ can reflect a sense of whether the A and B are preferred (positive $C_{A-B}(r^*)$) or avoided (negative) in the 1st-neighbor shell (a set of benchmark tests will be presented later).

In the ideal case, the projection columns in the EDS maps will be arranged regularly, with r^* as the interval. Then, the $C_{A-B}(r)$ curve would have values only at $r = r^*$, $2r^*$, $3r^*$, ... However, in experimental line profiles, although the atomic columns are overall distinguishable, there exist lattice distortion and peak straggling, which bring non-trivial noise to the correlation analysis if not taken care of. For example, the distance between adjacent columns can be widened to a range of distances, instead of a single distance of r^*. Thus, it is vital to robustly identify the exact location of each atomic column, and then extract the corresponding compositions to calculate the correlation coefficients. To this end, we develop the following procedure to locate the atomic columns in experimental line profiles:

(i) Interpolate a spline representation [42] of the discrete atomic concentration points for columns covered in an EDS line scan. The resultant concentration profile, $x_A(r)$, in the form of a spline, allows for the calculation of derivatives at any location;

(ii) Calculate the 1st derivative, $x'_A(r)$, and 2nd derivative, $x''_A(r)$.

(iii) Locate the A-enriched columns using $x'_A(r) = 0$, $x''_A(r) < 0$ and $x_A(r) > \overline{x_A}$. Here, $\overline{x_A}$ is the average of A concentration in the measured EDS regions. $x'_A(r) = 0 = 0$ and $x''_A(r) < 0$ are standard criteria to locate the local maxima, while $x_A(r) > \overline{x_A}$ filters out those local maxima with an atomic concentration lower than average (thus cannot be referred to as A-enriched columns).

Note that we only care about the local maxima, as the minima can either be from the element-depleted columns or from the void space between columns (which is not what we want), and for the former case, the column locations can be located from the local maxima of the other two elements. Later, when calculating the correlation coefficient, $C_{A-B}(r)$, we no longer use all the concentration values across the entire line profile, i.e., any pair of concentrations at two locations separated by any distance r; instead, we only use the concentrations corresponding to the identified atomic columns for the calculation of $C_{A-B}(r)$. The robustness of our correlation analysis is enhanced as a result.

3. Experimental results

3.1. Dual-phase microstructure

Fig. 1 shows the microstructural details after recrystallization annealing at 760 °C and 600 °C, respectively. Fig. 1a displays X-ray diffraction spectra for the two conditions, both indicating a dual-phase (DP) microstructure consisting of the face-centered-cubic (fcc) and hexagonal close-packed (hcp) structures. Fig. 1b and c are EBSD IPF micrographs, and Fig. 1d is the phase image. The fcc phase has a volume fraction of 98% after annealing at 760 °C and 82% at 600 °C, respectively, with an average grain size of 2.5 μm and 0.68 μm for fcc grains. Fig. 1e shows the composition distribution from the APT measurements. The concentration profiles show a uniform distribution of Fe, Mn, Co, and Cr elements inside the grain and across the grain boundary. These basic microstructural features are well consistent with those in the study by Li et al. [6], which was the first to report the design of this DP phase-transformation HEA.

3.2. CSRO observations

The CSRO regions are observed only in the fcc phase of the present DP HEA, which will be our focus in the rest of this article. The CSRO has been monitored after recrystallization at two temperatures of recrystallization annealing. The effect of subsequent tensile straining is also assessed.
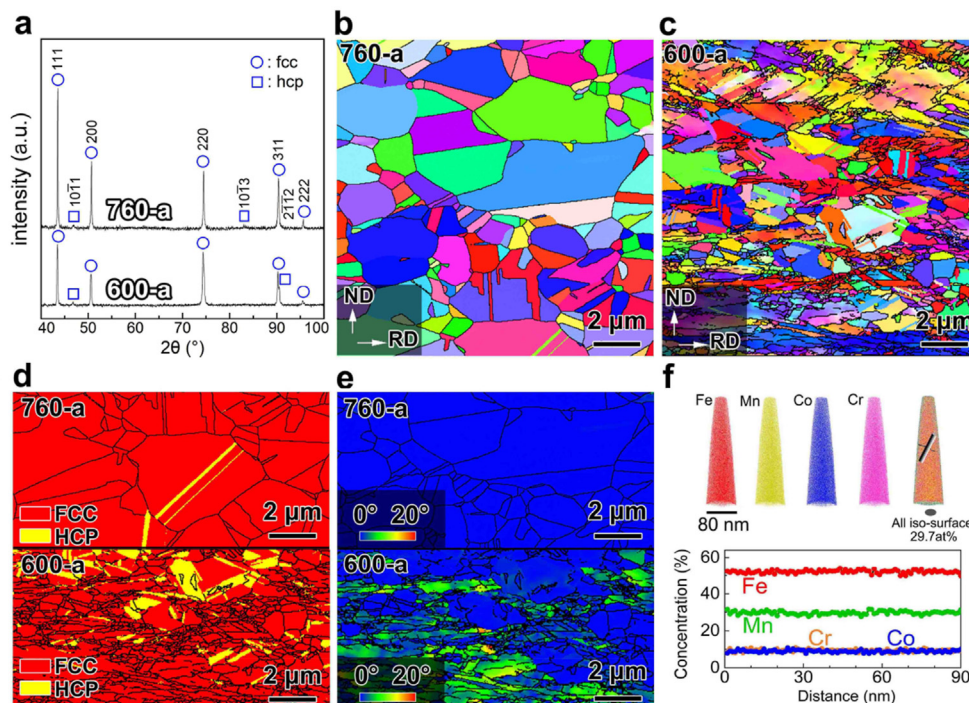
Fig. 1. Microstructure of Fe$_{50}$Mn$_{30}$Co$_{10}$Cr$_{10}$ (at%) high-entropy alloy after recrystallization annealing. (**a**) XRD spectra after annealing at 760 °C and 600 °C, labeled as 760-a and 600-a, respectively. Both are dual-phase of fcc and hcp structure. (**b**) and (**c**) Corresponding EBSD Inverse Pole Figure (IPF) in 760-a and 600-a, respectively. (**d**) and (**e**) EBSD phase images and grain reference orientation deviation (GROD) images for the two microstructures, respectively. (**f**) 3D APT tip reconstructions of Fe, Mn, Co, Cr atom positions along with 1D concentration profiles taken along the length direction of the tip shown in the inset. XRD, X-ray diffraction.

3.2.1. Electron diffraction evidence of CSRO

Fig. 2a is the HAADF image of the fcc phase after annealing at 760 °C (labeled as 760-a sample). The Fast Fourier Transform (FFT) pattern (inset in Fig. 2a) clearly exhibits extra *diffuse* reflections (one is circled in yellow as an example) in between the transmission spot (000) and the $\{\overline{3}11\}$ diffraction spots. This indicates the presence of additional ordering besides the fcc itself [14,33,36]. Of special note is the diameter of each diffuse disk in reciprocal space, which is almost one order of magnitude larger than that of Bragg spots. This indicates that the corresponding coherently scattering region in real space must be very small [33], so small that they are down to the length scale of CSROs.

Based on the FFT pattern, two inverse FFT (IFFT) images are obtained to observe the CSRO regions. One is the fcc lattice image obtained by using the normal fcc {311} spots (see Fig. 2b), while the other shows the CSRO regions using the diffuse disks (Fig. 2c, a few CSRO regions are circled in yellow). In both images, it is visible that lattice planes characterizing the periodicity of CSRO (red lines in Fig. 2c) have an inter-planar spacing (d_{CSRO}) that is twice the d_{fcc} of $\{\overline{3}11\}$ planes (red lines in Fig. 2b). This is, exactly, the reason why the extra reflections appear at the $\frac{1}{2}\{\overline{3}11\}$ positions in the FFT pattern (inset in Fig. 2a).

Another method is adopted to further ascertain the presence of CSRO regions. A separate set of nanobeam diffraction observations were performed, which is able to significantly improve the imaging contrast when compared to the selected-area mode. In addition to the expected fcc Bragg spots (indexed), the nanobeam EDP with the [112] z.a (Fig. 2d). shows easily discernible extra disks (in this nano beam case their sizes are determined by the size of convergent beam, and not by the feature size in real space), all lining up at the positions corresponding to $\frac{1}{2}\{\overline{3}11\}$, as marked using arrows. The CSRO regions light up in the dark-field image (Fig. 2e), taken using the extra disks. The observations of these extra disks in both the FFT

pattern and nanobeam EDP proves without a doubt that the fcc phase contains CSRO regions.

The same CSRO was also found after the 760-a sample was subjected to tensile pulling to 36% strain (760-s sample), and also in the sample after annealing at 600 °C (600-a sample). Fig. 3a shows, respectively, the FFT pattern (upper panel) and nano-beam EDP (middle panel) for the fcc phase in the 760-s sample. Both the patterns show the same extra diffuse disk as those shown in the inset of Fig. 2a and d. Using these two imaging methods, Fig. 3b and c are the corresponding IFFT and dark-field images, respectively, to show the CSRO regions. The lower panel in Fig. 3a is the FFT pattern in the 600-a sample, while Fig. 3d is the corresponding IFFT image. The CSRO regions are clearly seen.

Fig. 4a summarizes the statistic size distribution of CSRO regions. Several interesting results are noteworthy. First, both the size distribution and range of CSRO is basically identical for the measurements from both the IFFT and dark-field images (for both the 700-a and 700-s samples). This indicates that the two methods to observe the CSRO regions are both effective and mutually verifiable. Second, the average size of CSRO regions, $\overline{d}$, is 0.75 nm, almost unchanged in all three cases, which is larger than that of 0.55 nm in VCoNi MEA [14]. Third, the vast majority (90%) of CSRO regions is less than 1 nm in size. Finally, the areal fraction, f_{areal}, of CSRO regions is shown in Fig. 4b as measured from both the dark-field and IFFT images. There is a moderate reduction of f_{areal} from 0.22 to 0.17 after tensile deformation for the 760° C-a sample, and f_{areal} is ~0.18 in the 600-a sample.

3.2.2. EDS-mapping of CSRO

We now provide chemical information to discern what kind of CSRO is present by probing into the detailed arrangements of the four chemical species (Fe, Mn, Co, Cr) in the CSRO regions. To this end, EDS mapping was carried out based on HAADF imaging with the [112] z.a.
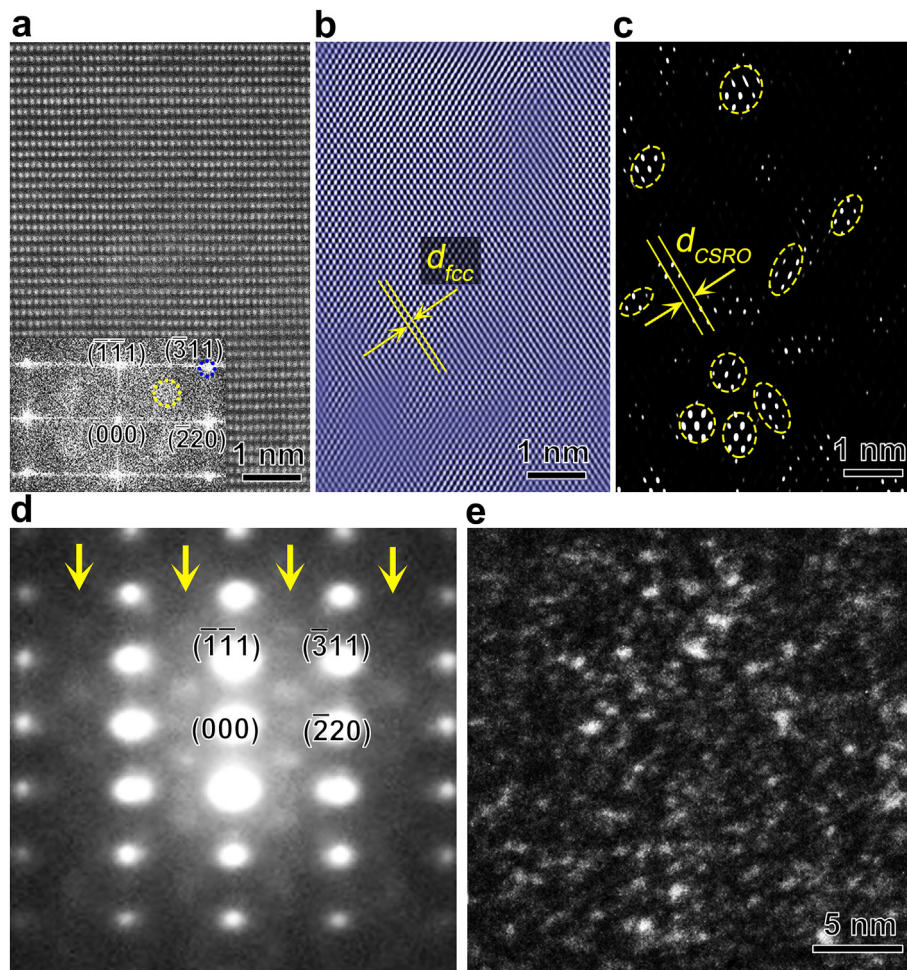
Fig. 2. Evidence of CSRO regions in the fcc phase of the 760 °C-annealed sample. (**a**) STEM-HAADF image of fcc phase with the [112] z.a. Inset: Fast Fourier Transform (FFT) pattern. Note the presence of extra *diffuse* reflections (one is labeled by a yellow dotted circle) at $\frac{1}{2}\{\bar{3}11\}$ positions, along with sharp Bragg spots from the fcc phase, e.g. $\bar{3}11$ diffraction labeled by a blue circle. (**b**) and (**c**) Inverse FFT (IFFT) images of the fcc lattice and CSRO regions, respectively, imaged using diffuse and $\bar{3}11$ diffractions. A few CSRO regions are circled in (c). The spacing of the $(\bar{3}11)$ plane is marked in both images. (**d**) Nanobeam EDP with the [112] z.a. Note the presence of arrays of extra reflections at $\frac{1}{2}\{\bar{3}11\}$ positions as pointed by arrows. (**e**) Energy-filtered dark-field TEM image taken using extra diffractions, showing the CSRO regions. CSRO, chemical short-range order; EDP, electron diffraction pattern; fcc, face-centered-cubic; TEM, transmission electron microscopy.
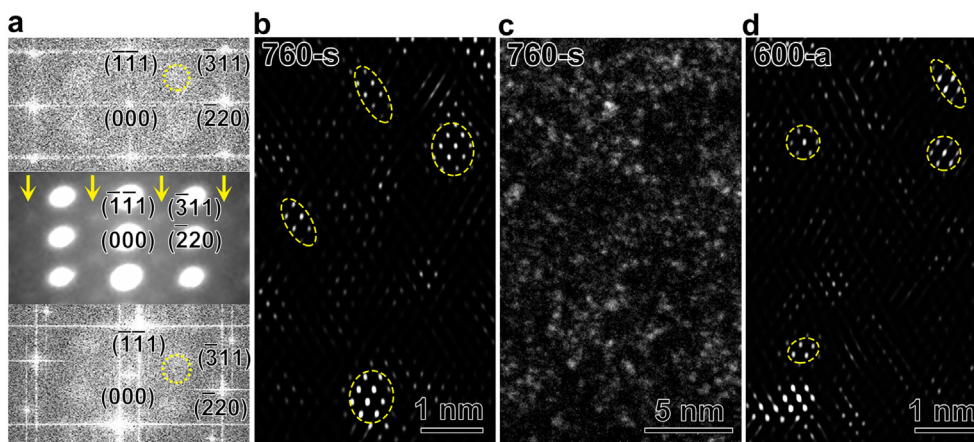

Fig. 3. CSRO regions in other samples/states. (**a**) FFT pattern and nano-beam electron diffraction pattern (EDP) of fcc phase (upper and middle panel) in the 760 °C-strained sample (labeled as 760-s) and FFT pattern (lower panel) in the 600 °C-annealed sample (labeled as 600-a). All with the [112] z.a. Yellow dotted circles indicate diffuse reflections at $\frac{1}{2}\{\bar{3}11\}$ positions in both FFT patterns. (**b**) and (**c**) IFFT image and energy-filtered dark-field image, respectively, showing the CSRO regions in the 760-s sample. (**d**) IFFT image showing circled CSRO regions in 600-a sample. CSRO, chemical short-range order; FFT, fast Fourier transform; IFFT, inverse FFT.
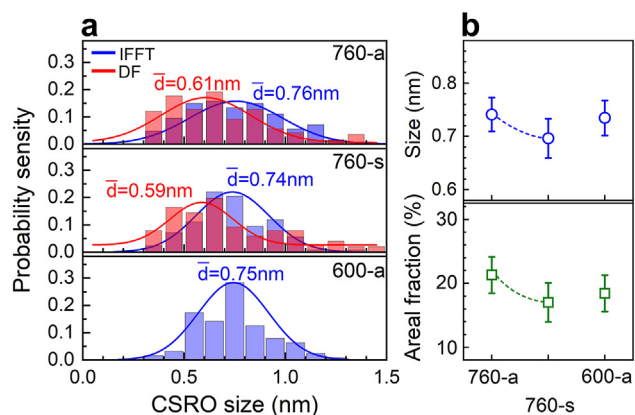
Fig. 4. Statistical size distribution and areal fraction of CSRO regions. (**a**) Size distribution of CSRO regions, together with the average size ($\bar{d}$), measured from both the IFFT and/or dark-field images in three samples, the 760 °C-annealed sample (labeled as 760-a), the 760 °C-strained sample after tensile deformation to 36% strain (labeled as 760-s) and the 600 °C-annealed sample (labeled as 600-a). (**b**) Average size and areal fraction. CSRO, chemical short-range order; IFFT, inverse fast Fourier transform.

Fig. 5a shows the EDS-map, in 760-a sample, for an individual element, i.e., Fe (red), Mn (green), Co (blue) and Cr (yellow) by line scanning across many atomic columns in a typical (111) plane along the [112] direction. The corresponding profiles of atomic concentration were summarized in Fig. 5b (its analysis will be presented in Section 3.3). Fig. 5c displays four EDS maps for individual and a pair of elements, i.e., Fe (red), Fe−Mn (red-green), Fe−Co, and Fe−Cr. Each spot corresponds to an atomic column along the thickness direction of TEM foil. The intensity (i.e., brightness) of colored spots depends on the make-up of the column, scaling with the content of the particular element being probed. Of special note is that the CSRO can be well described in terms of the preference for unlike species and avoidance of like pairs. For example, in Fig. 5c, two Fe-enriched ($\bar{3}$11) planes (solid white lines, across red spots) sandwich one Fe-depleted ($\bar{3}$11) plane (under dashed white lines, in either the FeCr or the FeCo or the FeMn map, across intense green/blue/yellow spots but faint or even vanishing red Fe). In other words, the ($\bar{3}$11) planes having more Fe content relative to the nominal sample Fe concentration alternate with those containing more Mn, Co and/or Cr with respect to the average of compositions. Such a chemical order has a period that doubles the interplanar spacing of fcc lattice. This explains again why the extra superlattice reflections appear at the locations which correspond to $\frac{1}{2}\{\bar{3}11\}$ (inset in Fig. 2a and d).
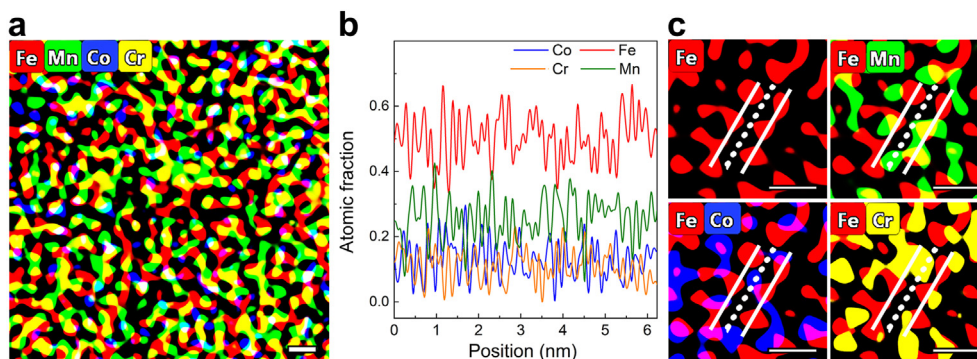
Namely, the CSRO regions are made up of the (Cr, Mn, Co)-enriched ($\bar{3}$11) planes interspersed with Fe-enriched planes in between. Furthermore, the alternating preferential chemical occupancy usually extends across only a few ($\bar{3}$11) planes (usually 3 to 5 atomic layers, as seen in Fig. 5c), i.e., a distance of less than 1 nm, well in line with the CSRO size (Fig. 4). Chemical ordered entities up to this length scale meet the definition of the CSROs.

Fig. 6 shows again the EDS-maps but in the 760-s sample. The preference/avoidance of species is very similar to what has been described previously. That is, in terms of the occupancy of the four elements in the CSRO regions, again two Fe (or Mn, Cr, Co)-enriched planes are apart by a distance twice the normal spacing of {$\bar{3}$11} planes in fcc lattice, as there is one Fe (or Mn, Cr, Co)-depleted plane in between.

3.3. Analysis of spatial correlation

We now come back to the concentration profile in Fig. 5b. While the concentration profiles seem to fluctuate randomly, CSRO may be hidden in the form of some specific fluctuation patterns. As detailed in Section 2.2, in a recent work [14], we have developed a set of spatial pair correlation coefficients to quantitatively gauge the ordering from the experimental EDS line profiles. We also deliberately synthesized several structural models with known CSROs to demonstrate the useful features of the $C_{A-B}(r)$ analysis framework. For an equiatomic VCoNi MEA [14], as an example, it has been proved that for the special quasi-random structure (SQS) [43] when no preferential ordering exists, $C_{A-B}(r^*)$ is close to 0, while for the structures with V−V avoided in the 1st-neighbor, $C_{A-B}(r^*)$ is negative (which is the most prominent ordering in the VCoNi MEA) [14]. In this work, we will also employ some synthetic structural models to demonstrate the suitability of the analysis for the present quaternary non-equiatomic $Fe_{50}Mn_{30}Co_{10}Cr_{10}$ HEA.

As a benchmark test, a 29,568-atom $Fe_{50}Mn_{30}Co_{10}Cr_{10}$ SQS structure was built by performing swap trials of different-species atoms until the Warren-Cowley order parameter in the 1st and 2nd neighbor shells are all close to 0. The sample dimension is ~7.0 nm (x) × 6.8 nm (y) × 7.1 nm (z), respectively, with x, y, and z along [11$\bar{2}$], [111], and [$\bar{1}$10] direction. Based on the EDS mapping for Fe, Mn, Co, and Cr along the [11$\bar{2}$] z.a. (Fig. 7a), we derive typical line scan profiles of a (111) plane along [$\bar{1}$10] direction as shown in Fig. 7b. Although there is no ordering preference in the SQS structure, the composition fluctuation in the projection columns is still significant. The pair correlations, $C_{A-B}(r)$, are then calculated
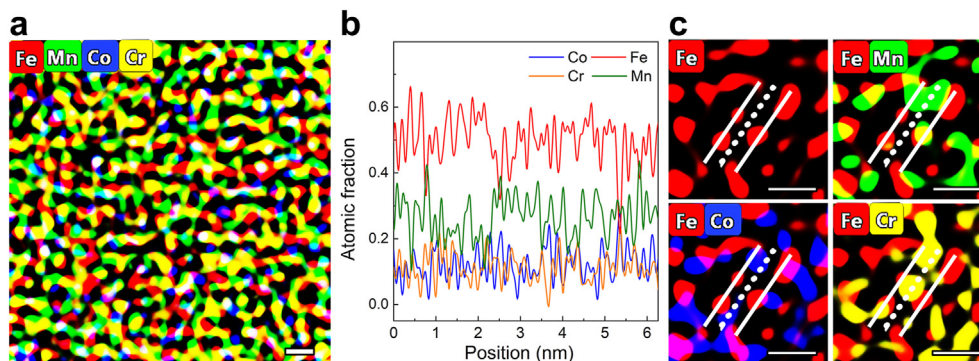

Fig. 5. EDS maps of the 760 °C-annealed sample. (**a**) EDS-map from the HAADF image with the [112] z.a. The brightness has been normalized for each species. (**b**) Line scan profile of atomic fraction. This atomic concentration is the average in each atomic column, and the concentration profile covers neighboring atomic columns, column by column, inside a typical {111} plane parallel to the <112> beam direction. (**c**) Close-up maps of Fe and corresponding binary map, indicating Fe enrichment on alternating atomic planes. Each white line marks the ($\bar{3}$11) plane intersecting the (111) plane in plan-view. Solid white line: Fe-enriched; dashed white line: Mn-/Co-/Cr-enriched. All scale bars are 0.25 nm. EDS, energy dispersive X-ray spectroscopy; HAADF, high-angle annular dark-field.

Fig. 6. EDS maps in the 760 °C-strained sample. (**a**) EDS-map from the HAADF image with the [112] z.a. (**b**) Line scan profile of atomic fraction. (**c**) Close-up maps of Fe and corresponding binary map, indicating Fe enrichment on alternating atomic planes. Each white line marks the ($\bar{3}$11) plane intersecting the (111) plane in plan-view. Solid white line: Fe-enriched; dashed white line: Mn-/Co-/Cr-enriched. All scale bars are 0.25 nm. EDS, energy dispersive X-ray spectroscopy.

using 30 line profiles (Fig. 7c). The $C_{A-B}(r^*)$ of all element pairs are close to 0 (Fig. 7c), indicating that there is no specific compositional covariation pattern and proving the absence of CSRO.

As a further test, a $Fe_{50}Mn_{30}Co_{10}Cr_{10}$ model structure with Fe−Fe being deliberately avoided was built. This is realized by using the Fe−Fe Warren-Cowley order parameter, α_{Fe-Fe}, as the target function, and swap trials are conducted, starting from SQS structure, to increase α_{Fe-Fe} (positive order parameter signifies avoidance; the order parameters between the other pairs are not monitored). Similar to that of the SQS structure (Fig. 7), Fig. 8 shows the EDS maps of Fe, Mn, Co, and Cr along the [11$\bar{2}$] zone axis, the typical line scan profiles of a (111) plane, and the Fe-related pair correlations for a $Fe_{50}Mn_{30}Co_{10}Cr_{10}$ structure with $\alpha_{Fe-Fe} = 0.10$. When compared with the case of the SQS structure (Fig. 7a and b), a similar degree of composition fluctuation is seen in the EDS maps and line profiles (Fig. 8a and b). However, the negative $C_{Fe-Fe}(r^*)$ and positive $C_{Fe-Mn/Co/Cr}(r^*)$ clearly reveals the existence of Fe−Fe avoidance and Fe−Mn/Co/Cr preference in the 1st neighboring

shell. Overall, such benchmark testing verifies the validity of this analytical framework on this quaternary non-equiatomic HEA.

As shown in Figs. 7 and 8, in the ideal case, the projection columns in the EDS maps are arranged regularly, with r^* as the interval, and the $C_{A-B}(r)$ curve has values only at $r = r^*$, $2r^*$, $3r^*$, ... In experimental line profiles, however, there is lattice distortion and peak straggling. The resultant spread-out of the position of each column needs to be minimized in numerical treatment, so that we can reliably correlate individual atomic columns. To this end, we developed a procedure to robustly locate the atomic columns in experimental line profiles (see Section 2.2 for details). Fig. 9a illustrates the identification of the atomic column locations in the Fe, Mn, Co and Cr concentration profiles along with an EDS line scan. The colored vertical lines show the locations of Fe-, Mn-, Co-, and Cr-enriched columns. Our efforts toward explicitly pinpointing the locations for the atomic columns enables more reliable analysis of the spatial correlation at the locations of interest− near the multiples of r^*.

After identifying the Fe-, Mn- and Co, and Cr-enriched columns and their locations, we first analyze whether these columns distribute with some pattern in space. Fig. 9b plots the distribution
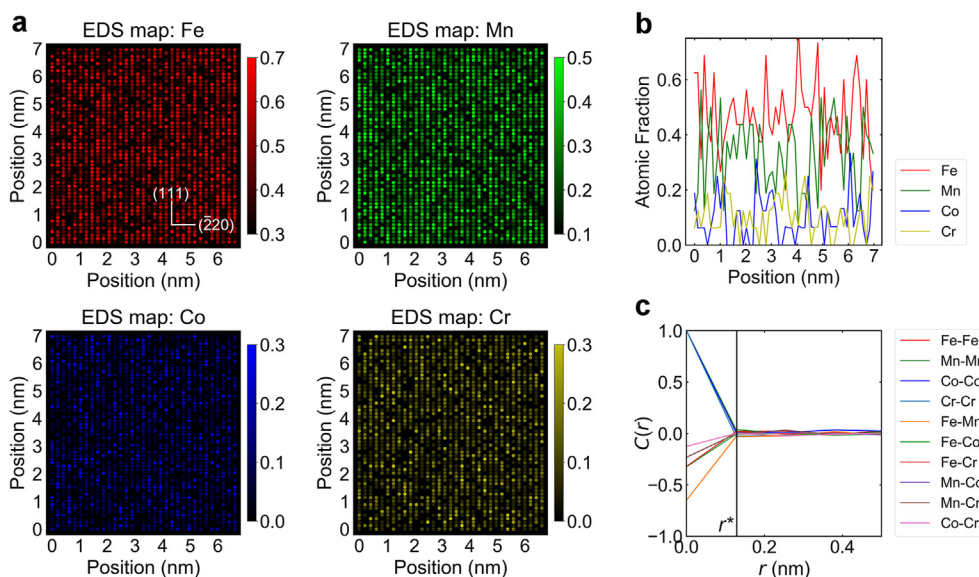

Fig. 7. Chemical mapping and spatial pair correlation simulated for a special quasi-random structure (SQS) $Fe_{50}Mn_{30}Co_{10}Cr_{10}$ sample. (**a**) EDS maps showing the element distribution of Fe, Mn, Co, and Cr. The projection is along [11$\bar{2}$] zone axis. (**b**) Typical line composition profile in a (111) plane (parallel to the e-beam direction). It shows obvious composition fluctuation from column to column, even though no preferential chemical ordering exists in this SQS sample. (**c**) Pair correlation coefficients, $C_{A-B}(r)$, calculated from 30 EDS line composition profiles. The location of r^*, namely the distance between adjacent columns in a projected (111) plane, is marked, and the corresponding $C(r^*)$ values are all close to 0, demonstrating the absence of any 1st-neighbor CSRO. CSRO, chemical short-range order; EDS, energy dispersive X-ray spectroscopy.
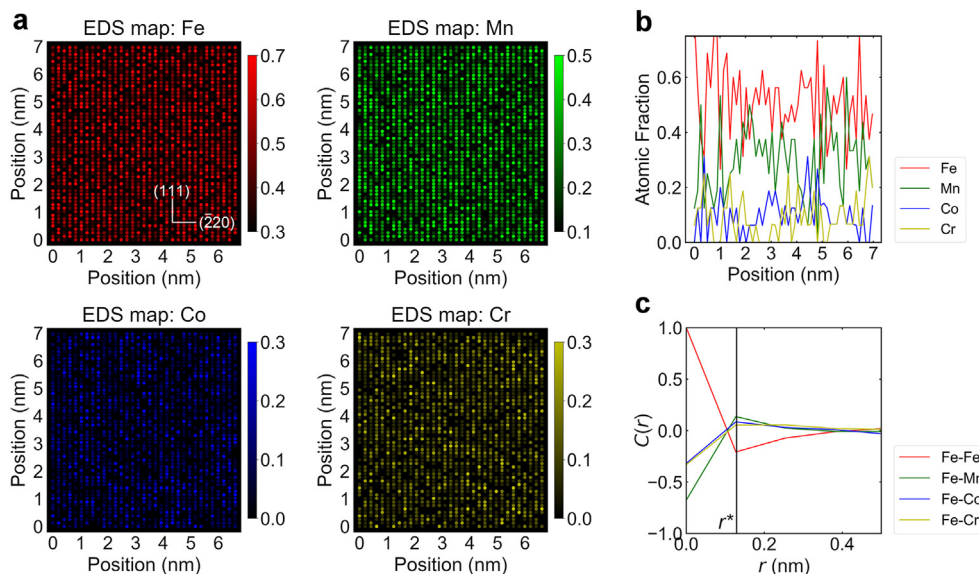
Fig. 8. **Chemical mapping and spatial pair correlation for a Fe$_{50}$Mn$_{30}$Co$_{10}$Cr$_{10}$ structure with Fe—Fe deliberately avoided.**(**a**) EDS maps showing element distribution of Fe, Mn, Co, and Cr. The projection is along $[11\bar{2}]$ zone axis. (**b**) Typical line composition profile in a (111) plane (parallel to the e-beam direction). (**c**) Pair correlation coefficients, $C_{Fe-A}(r)$, calculated from 30 EDS line composition profiles, where A = Fe, Mn, Co and Cr. The location of r^*, namely the distance between the adjacent columns in the given (111) plane, is marked, and the negative $C_{Fe-Fe}(r^*)$ and positive $C_{Fe-Mn/Co/Cr}(r^*)$ reveals the Fe—Fe avoidance in the 1st-neighbor CSRO. CSRO, chemical short-range order; EDS, energy dispersive X-ray spectroscopy.

of the distance between A-enriched and B-enriched columns from a total of 10 independent EDS lines, in the 760-a and 760-s samples, respectively. This probability density distribution is akin to the partial pair correlation function, $g_{A-B}(r)$, commonly used to gauge A-B pair distribution correlations in 3D atomic structures. Distinct peaks (maxima of humps) are observed before the distribution curve levels off at greater distances, and the locations of the 1st to 4th peaks are marked with dashed vertical lines (Fig. 9b).

Interestingly, we find the columns enriched with the same element, Fe—Fe, Mn—Mn, Co—Co and Cr—Cr, mostly contribute to the 2nd and 4th peaks, i.e., they are typically being separated by distances of $2r^*$ and $4r^*$; while the unlike species, Fe—Mn, Fe—Co, Fe—Cr, Mn—Co, Mn—Cr and Co—Cr, tend to be 1st-neighbor columns (at r^*), repeating at $3r^*$. This manifests the tendency toward like-pair avoidance and unlike-pair preference in the 1st neighboring shell, which is consistent with, and complements, the finding of the
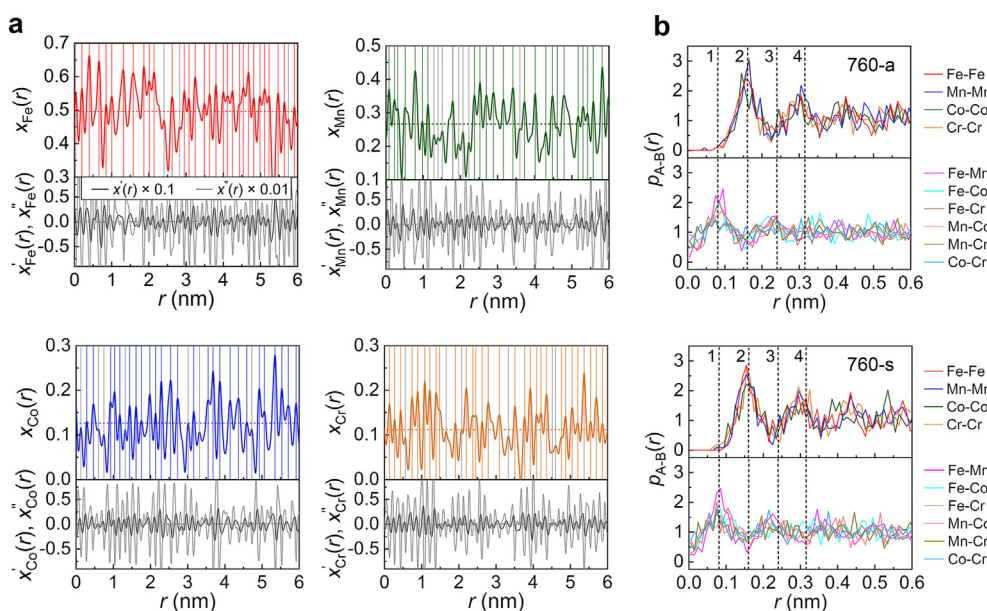

Fig. 9. **Identifying chemical ordering patterns from the profiles of atomic concentration obtained from the experimental line scans in EDS mapping.** (**a**) Determining the location of element-enriched columns from the EDS line profiles. The red, green, blue and orange vertical lines show the locations of Fe-, Mn-, Co- and Cr-enriched columns, and the gray lines are the excluded local maxima with concentration lower than the sample average of each element (the colored dotted horizontal line in the upper panel). The 1st derivative, $x'_A(r)$, and 2nd derivative, $x''_A(r)$, are presented for each concentration profile (lower panel). (**b**) The probability distribution for the distance between A-enriched and B-enriched columns (A, B = Fe, Mn, Co and Cr), from a total of 10 independent EDS lines, for the 760 °C-annealed sample (labeled as 760-a) and the 760 °C-strained sample (labeled as 760-s), respectively. The dashed vertical lines denote the center of four distinct peaks (maxima) observed. EDS, energy dispersive X-ray spectroscopy.
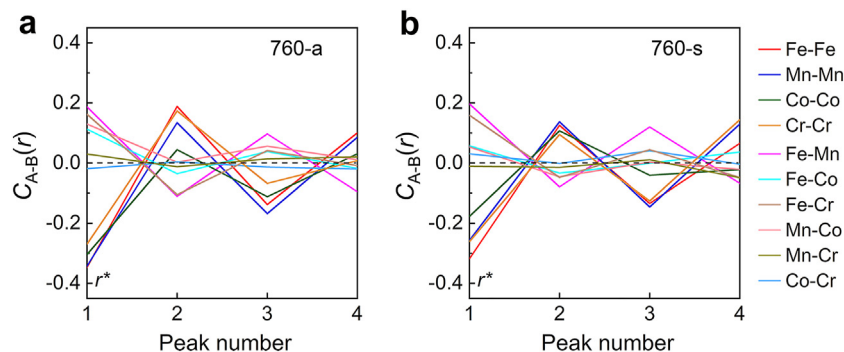
Fig. 10. Chemical ordering identified from experimental EDS profiles. Pair correlation coefficient curves, $C_{A-B}(r)$, between the ten element pairs, of (**a**) the 760 °C-annealed sample (labeled as 760-a) and (**b**) the 760 °C-strained sample (labeled as 760-s). Used in the calculations are concentration data from ten experimental EDS line profiles, each follow a 'line scan' along the $[\bar{1}10]$ direction, for atomic columns in a (111) plane projected along the in-plane $[11\bar{2}]$ zone axis. EDS, energy dispersive X-ray spectroscopy.

alternating A-enriched and A-depleted (B/C/D-enriched) (311) planes in Fig. 2. Such a trend persists both before and after plastic deformation (Fig. 9b).

We proceed to extract the pair correlation coefficients to quantitatively evaluate the strength of correlation between each element pair. As the locations of atomic columns have been identified above (Fig. 9a), we will use the concentrations corresponding to the identified atomic column locations to calculate $C_{A-B}(r)$. Because the distance between columns is actually a distribution (over a range) instead of a single number, the distance between columns is in the form of a 'peak envelope', each having a width and being bounded by the valleys on either side. Based on Fig. 9b, we designate the distance ranges of the 1st, 2nd, 3rd, and 4th peak and sample all the A-B concentration pairs within each peak, and use Eq. (1) to derive $C_{A-B}(r^*)$, $C_{A-B}(2r^*)$, $C_{A-B}(3r^*)$ and $C_{A-B}(4r^*)$. The $C_{A-B}(r)$ results of the 760-a sample are shown in Fig. 10a. In contrast to the SQS case (Fig. 7c), obvious peaks and valleys are observed in the experimental $C_{A-B}(r)$ curves. Let us take the standpoint of Fe and examine the spatial correlations with various species in Fig. 10a. When the like elements (i.e., Fe–Fe) are r^* apart, $C_{Fe-Fe}(r^*)$ is at a negative valley, indicating that this like pair prefers not to be so close by. Unlike species, on the other hand, attract each other, as Fe–Mn, Fe–Co, and Fe–Cr all show positive $C_{A-B}(r^*)$ peaks at r^*. This trend is also true when we take the perspective of Mn, Co, and Cr, respectively (except for Mn–Cr and Co–Cr which are close to random). Furthermore, the valleys (peaks) at r^* will flip to peaks (valleys) at $2r^*$, and an alternating 'up and down' $C_{A-B}(r)$ of major element pairs persists at the 1, 2, 3 and 4 peaks, in line with the observation in Fig. 9b. The correlation between atomic columns in {111} planes serves to demonstrate the 'like-pair avoidance and unlike-pair preference' tendency, forming a pattern that extends across several adjacent atomic columns. This analysis supports and expands from the visual observation in Fig. 5c toward a repeating Fe-enriched (i.e., Mn, Co, Cr depleted)/Fe-depleted (i.e., Mn, Co, Cr enriched) sequence in terms of chemical concentration.

After plastic straining in the 760-s sample, the amplitudes of $C_{A-B}(r^*)$ overall show a decrease (left panel in Fig. 10b). This suggests a decrease in the degree of CSRO, in line with the reduced areal fraction of CSRO after tensile straining (Fig. 4b). This suggests that plastic activities during straining can sometimes disrupt the local chemical ordering in the as-prepared alloy [26].

4. Discussion

To recapitulate our findings, the presence of CSROs is evidenced by electron diffraction patterns before and after tensile deformation showing extra diffuse reflections in between the transmission spot

(000) and $\{\bar{3}11\}$ diffraction spots in both the FFT patterns (inset in Figs. 2a and 3a) and nanobeam diffraction patterns (Fig. 2d), all with the [112] z.a. The spatial extent of the CSRO regions is clearly identified in the IFFT (Figs. 2c and 3b) and dark-field image (Figs. 2e and 3c). The EDS mapping further dissects the chemical order in terms of the preferred arrangements of the four chemical species (Fe, Mn, Co, Cr) across neighboring atomic planes (Fig. 5c).

Interestingly, our results above indicate that even though Cr, Mn, Fe, and Co are close in atomic size and the magnitudes of their heat of mixing are rather small, CSRO does develop in the quaternary HEA. What is even more intriguing is that the chemical ordering shows a pattern similar to that found in VCoNi MEA [14]: the alternating (311) planes and the 'preference for unlike pairs and avoidance of unlike pairs'; both continue to hold for the HEA. This similarity is a bit puzzling, because in VCoNi MEA, V is somewhat larger than Co and Ni, and intermetallic phases are known for the system (including a metastable trigonal VNi phase in the binary sub-system [44]). For Fe–Mn–Co–Cr, on the other hand, such a 'breeding ground' for developing the particular type of CSRO observed does not seem to exist. In other words, by comparison with VCoNi, at least in many local regions Fe seems to play the role of V while Mn, Cr, Co act like Co, Ni; but the reason for this (in comparison with other alternatives, other than Fe being the richest element in concentration) is unclear at present. An in-depth understanding of this issue demands careful energy computations with thorough analysis, which is beyond the scope of this experimental study. Compared to ternary MEAs, the addition of a fourth element increases the diversity of binding between elements. For example, four unlike pairs, i.e., Fe–Mn, Fe–Co, Fe–Cr and Mn–Co all exhibit a relatively strong tendency to be neighbors (Fig. 9), elevating the variability of atomic packing in the HEA.

Finally, we re-emphasize that although a number of studies over the past several years have been devoted to CSRO in H/MEAs, unequivocal experimental evidence has remained few and far between [13,31,32] until our very recent success in the VCoNi MEA [14]. In fact, several previous experiments [21,31] had to rely on indirect approaches, such as fitting of X-ray or neutron data, often requiring extensive computation to claim CSRO. A convincing demonstration of CSRO has been missing for any HEA containing more than three elements. This work fills this hole. We note here that our dataset here offers two specific advantages in proving CSRO in HEAs. First, in our case, the CSRO offers a detectable diffraction signal, allowing us to see coherent diffracting domains directly using dark-field imaging and prove that they are indeed short-ranged (sub-nanometer) in size in real space. In fact, based on definitive real-reciprocal space relationship/correspondence, we have clear and firm proof of the CSRO periodicity. Second, we have

direct chemical information as to how the constituent elemental species prefer to reside (in an alternative fashion) in the neighboring atomic planes or columns, directly demonstrating a tendency toward the like-pair avoidance and unlike-pair preference. We captured this information using atomic-resolution EDS analysis, together with the quantified pair correlation coefficients characterizing both the characteristic length scale and the strength of the spatial correlation. Such key information goes well beyond earlier work about the CSRO in HEAs.

The development of CSRO requires mostly short-range diffusion, such that we get to detect it in the as-prepared HEA. A kinetics study of CSRO evolution would be interesting, but must await extensive future work to figure out how to quantify the degree of CSRO accurately along the way of its evolution, for example, at different temperatures and times of aging heat treatment.

5. Concluding remarks

In sum, our firm identification of CSRO was made possible by exploiting the appropriate zone axis, nano beam diffraction, dark-field imaging, atomic-resolution HAADF-STEM with FFT and IFFT, and atomic-scale EDS composition map. We have presented in this article a quantitative analysis to analyze planar arrangements and spatial correlations of like and unlike nearest-neighbor pairs. Without interference from data fitting and associated artifacts, CSRO in the $Fe_{50}Mn_{30}Co_{10}Cr_{10}$ HEA has been irrefutably demonstrated. Although this HEA does not have an equiatomic composition sitting right in the middle of the phase diagram such as some prototypical HEAs, it is nevertheless still a HEA and one that showed superior mechanical properties [6]. Equi-atomic HEAs may contain a similar level of, or perhaps even more, CSROs, although because of the change in composition the CSROs may be of a different variety (in atomic configuration and ordering pattern). In general, we expect all solid solutions concentrated with a high content of solutes to contain CSROs to some degree/extent. In this regard, $Fe_{50}Mn_{30}Co_{10}Cr_{10}$ may serve as an extreme case; even in such a HEA in which all the constituent elements are close in atomic size and have rather small enthalpy of mixing, there is still detectable CSRO in this seemingly random (ideal) fcc solid solution.

Author contributions

Xiaolei Wu and En Ma conceived the ideas and supervised the project. Zhiying Cheng performed the HAADF and EDS mapping observations. Qi Wang conducted the pair correlation analysis and swap Monte Carlo simulations. Dong Liu, Jing Wang, Xuefei Chen and Fuping Yuan conducted tensile testing, X-ray diffraction, electron backscatter diffraction, and TEM observations. Ping Jiang prepared the materials, samples and heat treatments. All authors participated in the discussions. Xiaolei Wu and En Ma wrote the paper.

Declaration of competing interest

The authors declare that they have no known competing financial interests or personal relationships that could have appeared to influence the work reported in this paper.

Acknowledgments

References

[1] E.P. George, D. Raabe, R.O. Ritchie, High-entropy alloys, Nat. Rev. Mater. 4 (8) (2019) 515–534.
[2] Y.F. Ye, Q. Wang, J. Lu, C.T. Liu, Y. Yang, High-entropy alloy: challenges and prospects, Mater. Today 19 (6) (2016) 349–362.
[3] D.B. Miracle, O.N. Senkov, A critical review of high entropy alloys and related concept, Acta Mater. 122 (2017) 448–511.
[4] E.P. George, W.A. Curtin, C.C. Tasan, High entropy alloys: a focused review of mechanical properties and deformation mechanisms, Acta Mater. 188 (2020) 435.
[5] E. Ma, X.L. Wu, Tailoring heterogeneities in high-entropy alloys to promote strength-ductility synergy, Nat. Commun. 10 (2019) 5623.
[6] Z.M. Li, K.G. Pradeep, Y. Deng, D. Raabe, C.C. Tasan, Metastable high-entropy dual-phase alloys overcome the strength-ductility trade-off, Nature 534 (2016) 227–230.
[7] Z. Lei, X. Liu, Y. Wu, H. Wang, S. Jiang, S. Wang, X. Hui, Y. Wu, B. Gault, P. Kontis, D. Raabe, L. Gu, Q. Zhang, H. Chen, H. Wang, J. Liu, K. An, Q. Zeng, T.-G. Nieh, Z. Lu, Enhanced strength and ductility in a high-entropy alloy via ordered oxygen complexes, Nature 563 (2018) 546–550.
[8] T. Yang, Y.L. Zhao, W.P. Li, C.Y. Yu, J.H. Luan, D.Y. Lin, L. Fan, Z.B. Jiao, W.H. Liu, X.J. Liu, J.J. Kai, J.C. Huang, C.T. Liu, Ultrahigh-strength and ductile superlattice alloys with nanoscale disordered interfaces, Science 369 (6502) (2020) 427–432.
[9] B. Gludovatz, A. Hohenwarter, D. Catoor, E.H. Chang, E.P. George, R.O. Ritchie, A fracture-resistant high-entropy alloy for cryogenic applications, Science 345 (6201) (2014) 1153–1158.
[10] S.L. Wei, S.J. Kim, J.Y. Kang, Y. Zhang, Y.J. Zhang, T. Furuhara, E.S. Park, C.C. Tasan, Natural-mixing guided design of refractory high-entropy alloys with as-cast tensile ductility, Nat. Mater. 19 (2020) 1175–1181.
[11] M.X. Yang, D.S. Yan, F.P. Yuan, P. Jiang, E. Ma, X.L. Wu, Dynamically reinforced heterogeneous grain structure prolongs ductility in a medium-entropy alloy with gigapascal yield strength, Proc. Natl. Acad. Sci. U.S.A. 115 (2018) 7224–7229.
[12] Q. Ding, Y. Zhang, X. Chen, X. Fu, D. Chen, S. Chen, L. Gu, F. Wei, H. Bei, Y. Gao, M. Wen, J. Li, Z. Zhang, T. Zhu, R.O. Ritchie, Q. Yu, Tuning element distribution, structure and properties by composition in high-entropy alloys, Nature 574 (2019) 223–227.
[13] R.P. Zhang, S.T. Zhao, J. Ding, Y. Chong, T. Jia, C. Ophus, M. Asta, R.O. Ritchie, A.M. Minor, Short-range order and its impact on the CrCoNi medium-entropy alloy, Nature 581 (2020) 283–287.
[14] X.F. Chen, Q. Wang, Z.Y. Cheng, M.L. Zhu, H. Zhou, P. Jiang, L.L. Zhou, Q.Q. Xue, F.P. Yuan, J. Zhu, X.L. Wu, E. Ma, Direct observation of chemical short-range order in a medium-entropy alloy, Nature 592 (2021) 712–716.
[15] J.B. Cohen, M.E. Fine, Some aspects of short-range order, J. Phys. Radium 23 (1962) 749–762.
[16] Y. Wu, F. Zhang, X.Y. Yuan, H.L. Huang, X.C. Wen, Y.H. Wang, H.H. Wu, X.J. Liu, H. Wang, S.H. Jiang, Z.P. Lu, Short-range ordering and its effects on mechanical properties of high-entropy alloys, J. Mater. Sci. Technol. 62 (2021) 214–220.
[17] M. Widom, W.P. Huhn, S. Maiti, W. Steurer, Hybrid Monte Carlo/molecular dynamics simulation of a refractory metal high entropy alloy, Metall. Mater. Trans. A 45 (2014) 196–200.
[18] A. Tamm, A. Aabloo, M. Klintenberg, M. Stocks, A. Caro, Atomic-scale properties of Ni-based FCC ternary, and quaternary alloys, Acta Mater. 99 (2015) 307–312.
[19] L.J. Santodonato, Y. Zhang, M. Feygenson, C.M. Parish, M.C. Gao, R.J.K. Weber, J.C. Neuefeind, Z. Tang, P.K. Liaw, Deviation from high-entropy configurations in the atomic distributions of a multi-principal-element alloy, Nat. Commun. 6 (2015) 5964.
[20] P. Singh, A.V. Smirnov, D.D. Johnson, Atomic short-range order and incipient long-range order in high-entropy alloys, Phys. Rev. B 91 (2015) 224204.
[21] F.X. Zhang, S.J. Zhao, K. Jin, H. Xue, G. Velisa, H. Bei, R. Huang, J.Y.P. Ko, D.C. Pagan, J.C. Neuefeind, W.J. Weber, Y.W. Zhang, Local structure and short-range order in a NiCoCr solid solution alloy, Phys. Rev. Lett. 118 (2017) 205501.
[22] L. Koch, F. Granberg, T. Brink, D. Utt, K. Albe, F. Djurabekova, K. Nordlund, Local segregation versus irradiation effects in high-entropy alloys: steady-state conditions in a driven system, J. Appl. Phys. 122 (2017) 105106.
[23] A. Fernandez-Caballero, J.S. Wrobel, P.M. Mummery, D. Nguyen-Manh, Short-range order in high entropy alloys: theoretical formulation and application to Mo-Nb-Ta-V-W system, J. Phase Equilibria Diffus. 38 (2017) 391–403.
[24] Y. Ma, Q. Wang, C.L. Li, L.J. Santodonato, M. Feygenson, C. Dong, P.K. Liaw, Chemical short-range orders and the induced structural transition in high-entropy alloys, Scripta Mater. 144 (2018) 64–68.
[25] J. Ding, Q. Yu, M. Asta, R.O. Ritchie, Tunable stacking fault energies by tailoring local chemical order in CrCoNi medium-entropy alloys, Proc. Natl. Acad. Sci. U.S.A. 115 (2018) 8919–8924.

[26] Q.J. Li, H. Sheng, E. Ma, Strengthening in multi-principal element alloys with local-chemical-order roughened dislocation pathways, Nat. Commun. 10 (2019) 3563.

[27] H.S. Oh, S.J. Kim, K. Odbadrakh, W. Ha Ryu, K.N. Yoon, S. Mu, F. Kormann, Y. Ikeda, C.C. Tasan, D. Raabe, T. Egami, E.S. Park, Engineering atomic-level complexity in high-entropy and complex concentrated alloys, Nat. Commun. 10 (2019) 2090.

[28] B.L. Yin, S. Yoshida, N. Tsuji, W.A. Curtin, Yield strength and misfit volumes of NiCoCr and implications for short-range-order, Nat. Commun. 11 (2020) 2507.

[29] W.R. Jian, Z.C. Xie, S.Z. Xu, Y.Q. Su, X.H. Yao, I.J. Beyerlein, Effects of lattice distortion and chemical short-range order on the mechanisms of deformation in medium entropy alloy CoCrNi, Acta Mater. 199 (2020) 352−369.

[30] C.G. Schön, On short-range order strengthening and its role in high-entropy alloys, Scripta Mater. 196 (2021) 113754.

[31] J.B. Seol, J.W. Bae, J.G. Kim, H. Sung, Z. Li, H.H. Lee, S.H. Shim, J.H. Jang, W.-S. Ko, S.I. Hong, H.S. Kim, Short-range order strengthening in boron-doped high-entropy alloys for cryogenic applications, Acta Mater. 194 (2020) 366−377.

[32] J. Moon, S.I. Hong, J.B. Seol, J.W. Bae, J.M. Park, H.S. Kim, Strain-rate sensitivity of high-entropy alloys and its significance in deformation, Mater. Res. Lett. 7 (2019) 503−509.

[33] D.B. Williams, C.B. Carter, Transmission Electron Microscopy, A Textbook for Materials Science, 233 Spring Street, Springer ScienceþBusiness Media, LLC, New York, NY 10013, USA, 2009.

[34] A. Marucco, B. Nath, Effects of ordering on the properties of Ni-Cr alloys, J. Mater. Sci. 23 (1988) 2107−2114.

[35] N. Kuwano, N. Chiwata, K. Oki, In situ TEM observation of long range ordering via short range order in Cu3Pt, Bull. Mater. Sci. 22 (1999) 697−700.

[36] G. Van Tendeloo, S. Amelinckx, The origin of diffuse intensity in electron diffraction patterns, Phase Transitions 67 (1998) 101−135.

[37] J.P. Chevalier, W.M. Stobbs, Short-range order and the disorder-order transformation in stoichiometric Ni4Mo, Acta Metall. 27 (7) (1979) 1197−1217.

[38] Y.S. Kim, W.Y. Maeng, S.S. Kim, Effect of short-range ordering on stress corrosion cracking susceptibility of Alloy 600 studied by electron and neutron diffraction, Acta Mater. 83 (2015) 507−515.

[39] J.B. Seol, J.G. Kim, S.H. Na, C.G. Park, H.S. Kim, Deformation rate controls atomic-scale dynamic strain aging and phase transformation in high Mn TRIP steels, Acta Mater. 131 (2017) 187−196.

[40] R. Zhang, S. Zhao, C. Ophus, Y. Deng, S.J. Vachhani, B. Ozdol, R. Traylor, K.C. Bustillo, J.W. Morris Jr., D.C. Chrzan, M. Asta, A.M. Minor, Direct imaging of short-range order and its impact on deformation in Ti-6Al, Sci. Adv. 5 (2019), eaax2799.

[41] K. Ohshima, D. Watanabe, Electron diffraction study of short-range-order diffuse scattering from disordered Cu−Pd and Cu−Pt alloys, Acta Cryst. A 29 (5) (1973) 520−526.

[42] C.R. Harris, K.J. Millman, S.J.V.D. Walt, R. Gommers, P. Virtanen, D. Cournapeau, E. Wieser, J. Taylor, S. Berg, N.J. Smith, R. Kern, M. Picus, S. Hoyer, M.H.V. Kerkwijk, M. Brett, A. Haldane, J.F.D. Rio, M. Wiebe, P. Peterson, P.G. Marchant, K. Sheppaard, T. Reddy, W. Weckesser, H. Abbasi, C. Gohlke, T.E. Oliphant, Array programming with NumPy, Nature 585 (2020) 357−362.

[43] A. Zunger, S.H. Wei, L.G. Ferreira, J.E. Bernard, Special quasirandom structures, Phys. Rev. Lett. 65 (1990) 353.

[44] https://materialsproject.org/materials/mp-1216313/.